Supplementary Information

Supplementary Text 1

The GFED5-based reconstruction data version

As sensitivity test of methods in this study, besides the FireCCI51-based reconstruction, we also used burned area from GFED5 to reconstruct global monthly burned area maps with half-degree spatial resolution from 1901 to 2020. The procedures are the same as methods using FireCCI51 mentioned in the main text.

In the model evaluation based on the leave-one-year-out method, the multi-year (2003-2020) mean burned area fraction (BAF) between observation (GFED5) and our prediction is spatially consistent in general (Fig. S18). There is a strong spatial correlation between observations and prediction at the global scale with R^2 of 0.99 and a linear slope of 0.97 (Fig. S18a). Among all regions, R^2 ranges from 0.80 to 0.99, and slopes range from 0.81 to 0.97 (Fig. S18c-q), which indicates that the trained models can well reproduce the spatial patterns of burned area.

Additionally, our models reproduced the inter-annual variability of GFED5 well (Fig. S19). R^2 from the temporal regressions of global total burned area between predictions and observations is 0.91, and it ranges from 0.49 to 0.95 across regions. The linear slope is 0.79 for the global total burned area, and its range is 0.59-0.96 across regions. The model can also well capture the seasonality of burned area in each region (Fig. S20).

Supplementary Text 2

The FireCCI51-GDP data version

We calibrated the reconstructed burned area before 2000 at the regional scale using GDP as a proxy of anthropogenic effects (e.g., fire suppression, landscape fragmentation). The workflow of the calibration processes is illustrated in Fig. S24. We first calculated the annual regional GDP based on the annual national GDP from the Maddison Project Database 2023 (Bolt and Van Zanden, 2024) in all countries in a given region. We then derived annual regional total burned area (BA) from (Mouillot and Field, 2005)). Among the 14 GFED regions, significant (p-value<0.05) linear correlations were found between the regional decade-averaged GDP and burned area (the BA-GDP linear correlation) in TENA, CEAM, NHSA, SHSA, NHAF, SEAS, EQAS and AUST (Fig. S25). We only selected these regions with a significant BA-GDP correlation to calibrate the original FireCCI51-based burned area using GDP, and burned area in regions without a significant correlation remained unchanged. Decades in the calibration process refer to 1901-1910, 1911-1920, …, and 1991-1999. Because GDP data in some regions were not available before 1950 in the Maddison Project Database 2023 (Bolt and Van Zanden, 2024), we reconstructed the regional GDP in the earlier periods using a linear regression. Specifically, in regions without annual GDP available before 1950, regional annual GDP in the earliest accessible 5 years were fitted against years using a linear regression. This regression was further applied to reconstruct the GDP in the earlier years. If the regional annual GDP was predicted to be negative by the linear regression, the regional annual GDP was assumed to be the same as the nearest year (Fig. S26).

In the FireCCI51-GDP data version, the decadal average of regional total BA was derived from

the BA-GDP regressions, while the annual anomalies were from the original FireCCI51-based reconstruction. A ratio of monthly BA to annual total BA from the original FireCCI51-based reconstruction was then applied to correct the monthly BA data in the FireCCI51-GDP version.

Finally, the regional total monthly BA after calibration by GDP was applied proportionally to each grid cell based on the gridded burned area from the original FireCCI51-based version.

Supplementary Text 3

Sensitivity tests of including lightning and terrain as explanatory variables

Lightning and terrain have been proved as basic and important information for understanding and predicting fire activity (Bowman et al., 2009; Bowman et al., 2020), we thus did sensitivity tests by including lightning and terrain as explanatory variables in the machine learning models.

We extracted the average of cloud-to-ground lightning power within 0.5°×0.5° grid cells for from The World Wide Lightning Location Network (WWLLN) Global Lightning Climatology (WGLC) and time series, which is a global dataset covering 2010-2024 at a spatial resolution of half-degree or 5 arc-minute (Kaplan and Lau, 2021). We then calculated the average and standard deviation of elevation, the median and standard deviation of slope gradient within 0.5°×0.5° grid cells based on Global Multiple Terrain Elevation Data (GMTED), a global dataset in 2010 at a spatial resolution up to 7.5 arc-second (Danielson and Gesch, 2011).

To save the computational cost in the sensitivity tests, we randomly selected a half of samples from 2010 to 2020 and then split it into the training set (80%) and the testing set (20%) in each region, respectively. In 0.5°×0.5° grid cells, we added the average cloud-to-ground lightning power to represent lightning, and the average and standard deviation of elevation, the median and standard deviation of slope gradient to represent terrain as explanatory variables in addition to the original variables (Table 1) in model training and testing.

Our sensitivity results show that lightning and terrain generally manifest minor effect across all regions in classification (Table S3). For regression, lightning and terrain pose considerable impacts in NHAF and SHAF but minor effects in other regions (Table S4, S5). Lightning improved the regression model performance in NHAF for regular burned area (R^2 improved by ~0.1, Table S4). In contrast, terrain decreased the regression model performance the most in SHAF for regular burned area (R^2 decreased by ~0.05, Table S4), but it increased the regression model performance in NHAF and SHAF for extreme burned area (R^2 improved by ~0.05, Table S5).

Despite the importance in some regions, we did not use lightning data for historical burned area reconstruction due to the limited time span. The time span of global lightning data is 2010-2024 (Kaplan and Lau, 2021), and the historical lightning data is not accessible especially before the 21st century. Terrain resampling to 0.5°×0.5° grid cells inevitably diluted explicit information from fine spatial resolution (Cary et al., 2006), which may partly explain its minor effect across all regions except NHAF and SHAF.

Table S1. Evaluation of the random forest classification models using the 20% testing set from all years' data (2003-2020). The data over the period of 2003-2020 was split into the training set (80%) and the testing set (20%) in each region. AUC represents Area Under receiver operating characteristic Curves ranging in 0-1, and a larger AUC value indicates better model performance. BAF is burned area fraction in each 0.5°×0.5° grid cell.

Region	Accuracy	AUC (regular BAF)	AUC (extreme BAF)
BONA	97.1%	0.936	0.973
TENA	89.8%	0.851	0.917
CEAM	90.3%	0.909	0.958
NHSA	90.6%	0.936	0.987
SHSA	88.1%	0.908	0.976
EURO	95.5%	0.947	0.966
MIDE	97.7%	0.972	0.968
NHAF	90.9%	0.961	0.989
SHAF	87.8%	0.941	0.984
BOAS	95.1%	0.939	0.971
CEAS	93.1%	0.930	0.968
SEAS	93.3%	0.946	0.988
EQAS	92.1%	0.888	0.950
AUST	87.9%	0.885	0.953

Table S2. Significant trends of annual total burned area from this study, FireCCILT11 and Mouillot and Field (2005) at the global scale and in each region. The trends (unit: million km^2 yr^{-2}) in Table S2 are summarized from Fig. 5 and Fig. 8. Similar trends in the overlapped periods from various datasets are marked in bold colors (red and blue for positive and negative trends, respectively).

Regions	Trend in this study	Trend in FireCCILT11	Trend in Mouillot and Field (2005)
Global	-0.009 (1901-1978) **0.020 (1978-2008)** **-0.050 (2008-2020)**	**0.025 (1995-2011)** **-0.113 (2011-2018)**	**0.041 (1972-1997)**
BONA	0.0003 (1901-1929) **-0.0002 (1929-2017)**	**-0.0002 (1996-2018)**	-0.003 (1901-1920) **-0.0004 (1920-1965)** 0.0008 (1965-1999)
TENA	**0.00005 (1901-1990)** -0.0002 (1993-2020)	**0.001 (1982-1991)**	-0.018 (1901-1909) -0.003 (1909-1965) **0.0003 (1965-1999)**
CEAM	0.00005 (1901-1995) 0.0009 (1995-2004) **-0.0002 (2004-2020)**	-0.0025 (1995-2001) **-0.0001 (2001-2018)**	-0.005 (1901-1905) -0.0002 (1905-1952) 0.0007 (1952-1999)
NHSA	**0.003 (1954-1960)** -0.0003 (1960-2020)	-	**0.0002 (1901-1970)** 0.003 (1970-1989) 0.002 (1989-1999)
SHSA	0.001 (1901-1962) -0.021 (1962-1974) **0.004 (1974-2020)**	-0.007 (1982-1992) **0.009 (1995-2004)** -0.003 (2004-2018)	-0.004 (1901-1934) -0.0003 (1934-1973) **0.014 (1973-1999)**
EURO	0.00002 (1901-1978) 0.0002 (1978-1991) -0.0002 (1991-2020)	0.0007 (1995-2012) -0.002 (2012-2018)	-0.00002 (1901-1971) 0.0005 (1971-1980) -0.0001 (1980-1999)
MIDE	0.00001 (1901-1985) 0.0003 (1985-1994) **0.00001 (1994-2020)**	**0.0006 (1995-2017)**	-0.00003 (1901-1999)
NHAF	**0.005 (1901-1922)** -0.008 (1922-1957) **-0.004 (1957-2020)**	**-0.019 (2007-2018)**	**0.004 (1901-1977)** 0.014 (1977-1999)
SHAF	-0.004 (1901-1979) **0.011 (1979-2011)** **-0.019 (2011-2020)**	**0.022 (1995-2012)** **-0.087 (2012-2018)**	-
BOAS	-0.0006 (1901-1941) 0.0009 (1941-1997) -0.0009 (1997-2020)	-	0.021 (1901-1915) -0.0001 (1915-1999)
CEAS	**0.0024 (1956-2006)** **-0.005 (2006-2020)**	**0.016 (1995-2002)** **-0.007 (2002-2018)**	-0.002 (1953-1981) **0.009 (1981-1999)**
SEAS	**-0.0002 (1901-1994)** **0.0014 (1994-2020)**	0.001 (1985-1993) **0.001 (1998-2018)**	**-0.004 (1901-1916)** 0.002 (1916-1968) **0.005 (1968-1999)**

EQAS	-	-	0.0002 (1901-1964) 0.002 (1964-1999)
AUST	**-0.0026 (1979-2020)**	-	**-0.006 (1936-1999)**

Table S3. Evaluation of the random forest classification models using original 16 explanatory variables (Table 1) (original) and adding lightning or terrain into explanatory variables respectively in each region. Note that Area Under receiver operating characteristic Curves (AUC) ranging in 0-1, and larger AUC indicating better model performance. Colored grids represent improved (red) or decreased (blue) model performance by adding lightning and terrain as explanatory variables compared to using original explanatory variables.

region	original			adding lightning			adding terrain		
	overall accuracy	AUC for regular BAF	AUC for extreme BAF	overall accuracy	AUC for regular BAF	AUC for extreme BAF	overall accuracy	AUC for regular BAF	AUC for extreme BAF
BONA	0.96	0.92	0.92	0.96	0.93	0.95	0.97	0.93	0.92
TENA	0.91	0.84	0.92	0.90	0.83	0.90	0.91	0.86	0.93
CEAM	0.90	0.89	0.95	0.90	0.89	0.94	0.89	0.89	0.95
NHSA	0.90	0.92	0.99	0.90	0.93	0.99	0.90	0.93	0.99
SHSA	0.87	0.89	0.98	0.87	0.89	0.97	0.88	0.90	0.98
EURO	0.98	0.95	0.96	0.98	0.95	0.95	0.98	0.96	0.97
MIDE	0.98	0.97	0.97	0.98	0.97	0.95	0.98	0.97	0.95
NHAF	0.90	0.96	0.99	0.89	0.95	0.99	0.90	0.96	0.99
SHAF	0.88	0.94	0.98	0.88	0.94	0.98	0.88	0.94	0.98
BOAS	0.95	0.93	0.96	0.95	0.94	0.96	0.96	0.94	0.96
CEAS	0.94	0.92	0.96	0.94	0.92	0.96	0.94	0.93	0.96
SEAS	0.92	0.93	0.98	0.92	0.93	0.98	0.93	0.94	0.98
EQAS	0.91	0.88	0.95	0.92	0.88	0.94	0.90	0.88	0.95
AUST	0.87	0.88	0.95	0.87	0.88	0.95	0.88	0.88	0.95

Table S4. Evaluation of the long short-term memory (LSTM) regression models using original 16 explanatory variables (Table 1) (original) and adding lightning or terrain into explanatory variables respectively for regular burned area in each region. R^2, slope, and RMSE represents the coefficients of determination, linear slope and rooted mean squared error between prediction and observation in the testing set. Colored grids represent improved (red) or decreased (blue) model performance by adding lightning or terrain as explanatory variables compared to using original explanatory variables.

Region	original			adding lightning			adding terrain		
	R^2	slope	RMSE	R^2	slope	RMSE	R^2	slope	RMSE
BONA	0.85	0.44	0.004	0.86	0.46	0.003	0.85	0.42	0.005
TENA	0.92	0.43	0.001	0.91	0.42	0.002	0.92	0.44	0.001
CEAM	0.64	0.43	0.002	0.65	0.47	0.002	0.66	0.48	0.002
NHSA	0.66	0.45	0.004	0.66	0.45	0.004	0.68	0.45	0.004
SHSA	0.83	0.50	0.002	0.83	0.50	0.002	0.84	0.55	0.002
EURO	0.91	0.45	0.001	0.91	0.46	0.001	0.91	0.47	0.001
MIDE	0.86	0.43	0.001	0.86	0.43	0.001	0.87	0.43	0.001
NHAF	0.77	0.58	0.019	0.87	0.68	0.011	0.75	0.55	0.019
SHAF	0.77	0.62	0.017	0.80	0.64	0.015	0.72	0.55	0.018
BOAS	0.65	0.33	0.005	0.65	0.34	0.005	0.67	0.35	0.004
CEAS	0.73	0.30	0.002	0.72	0.30	0.002	0.73	0.32	0.002
SEAS	0.71	0.35	0.004	0.72	0.35	0.004	0.73	0.35	0.004
EQAS	0.98	0.41	0.001	0.98	0.43	0.001	0.98	0.44	0.001
AUST	0.80	0.45	0.011	0.81	0.45	0.010	0.81	0.45	0.010

Table S5. Same as Table S4 but for extreme burned area.

Region	original			adding lightning			adding terrain		
	R^2	slope	RMSE	R^2	slope	RMSE	R^2	slope	RMSE
BONA	0.86	0.47	0.07	0.88	0.54	0.05	0.86	0.52	0.07
TENA	0.87	0.46	0.03	0.87	0.46	0.03	0.87	0.51	0.03
CEAM	0.96	0.41	0.02	0.96	0.41	0.02	0.96	0.45	0.02
NHSA	0.67	0.39	0.03	0.67	0.41	0.03	0.67	0.39	0.03
SHSA	0.78	0.41	0.06	0.78	0.43	0.06	0.78	0.41	0.06
EURO	1.00	0.40	0.01	1.00	0.40	0.01	1.00	0.40	0.01
MIDE	0.96	0.42	0.01	0.96	0.42	0.01	0.96	0.42	0.01
NHAF	0.65	0.51	0.16	0.67	0.51	0.15	0.70	0.55	0.15
SHAF	0.65	0.46	0.13	0.62	0.42	0.14	0.70	0.47	0.12
BOAS	0.58	0.44	0.08	0.59	0.51	0.07	0.60	0.50	0.08
CEAS	0.86	0.46	0.06	0.86	0.44	0.06	0.87	0.46	0.06
SEAS	0.68	0.48	0.06	0.68	0.48	0.06	0.60	0.45	0.07
EQAS	0.88	0.40	0.01	0.88	0.37	0.01	0.89	0.40	0.01
AUST	0.67	0.43	0.13	0.69	0.45	0.12	0.68	0.46	0.13

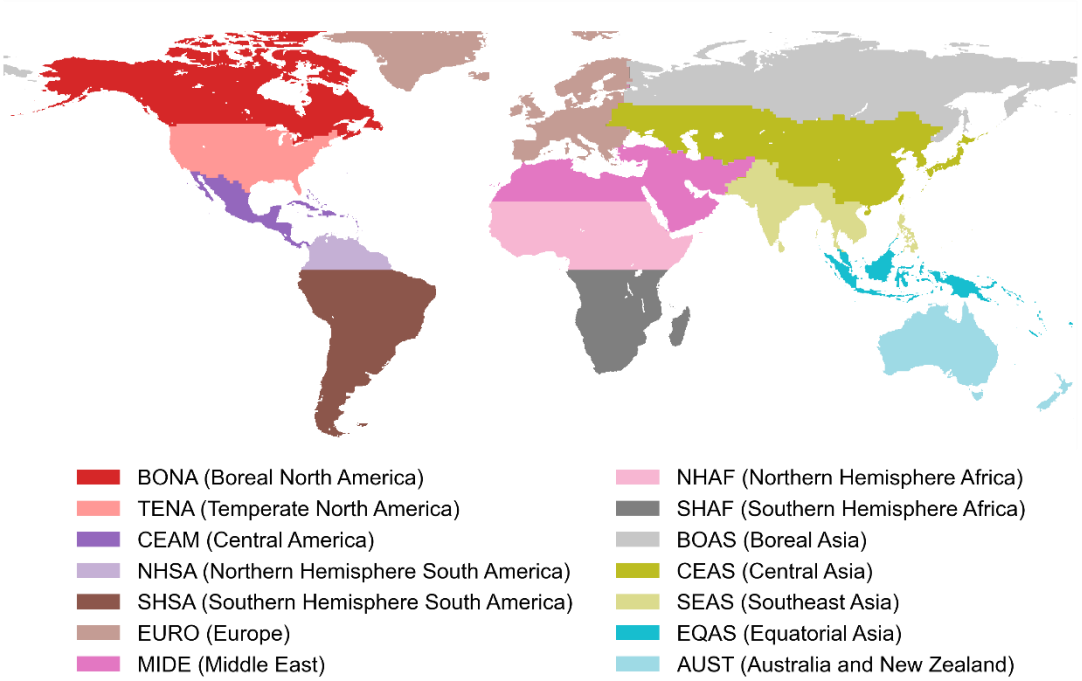

Figure S1. Map of GFED regions used in this study following (Van Der Werf et al., 2017).

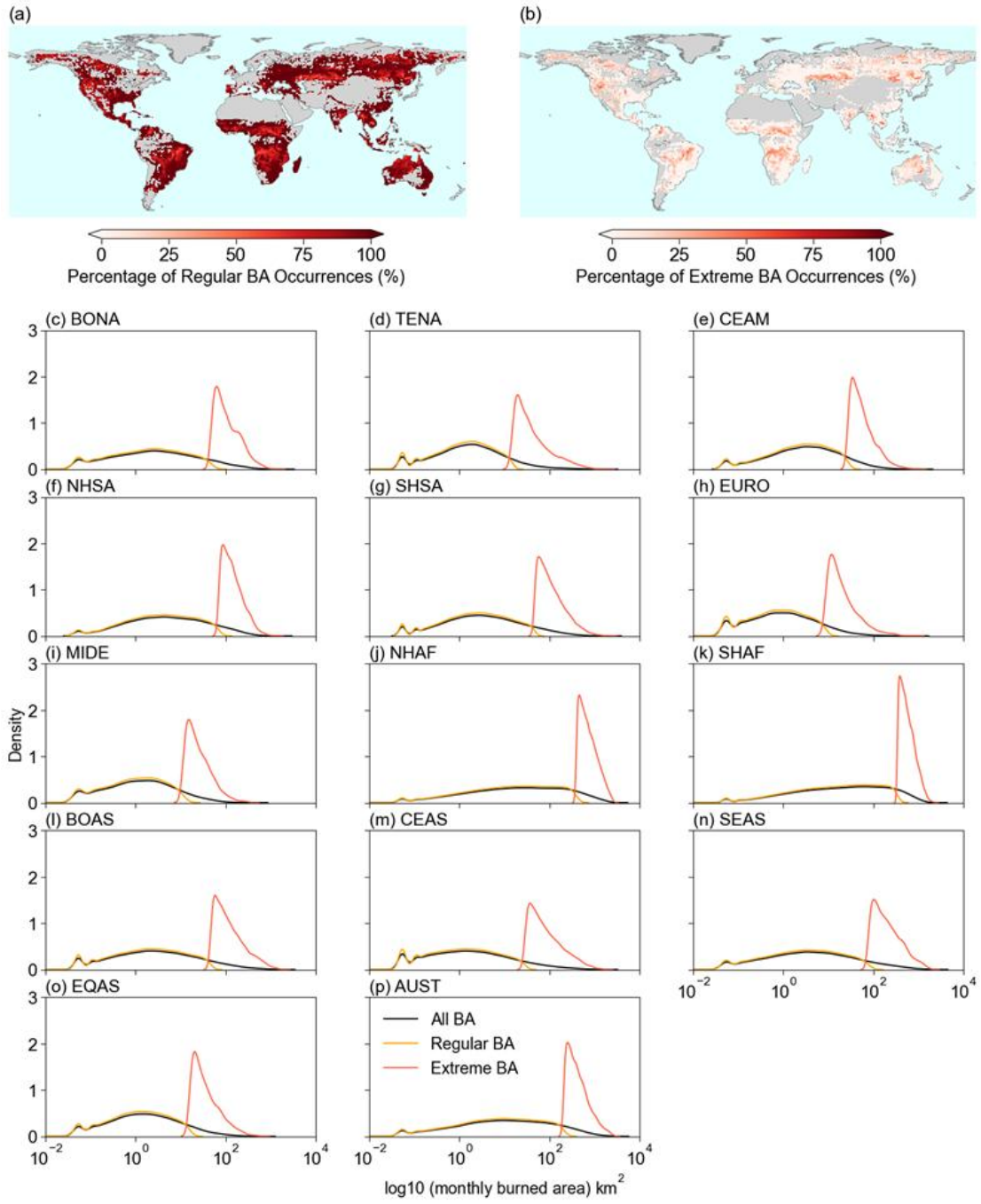

Figure S2. Distribution of regular and extreme monthly burned area within half-degree grid cells based on FireCCI51 in 2003-2020. (a-b) Spatial distribution of fire occurrence (%) (i.e., the number of months with fire occurrence divided by the total month number in 2003-2020 multiplying 100%) for the regular and extreme burned area. (c-p) Kernel density distribution of monthly burned area within half-degree grid cells in 2003-2020 for all (black lines), regular (orange lines) and extreme (red lines) burned area in various regions.

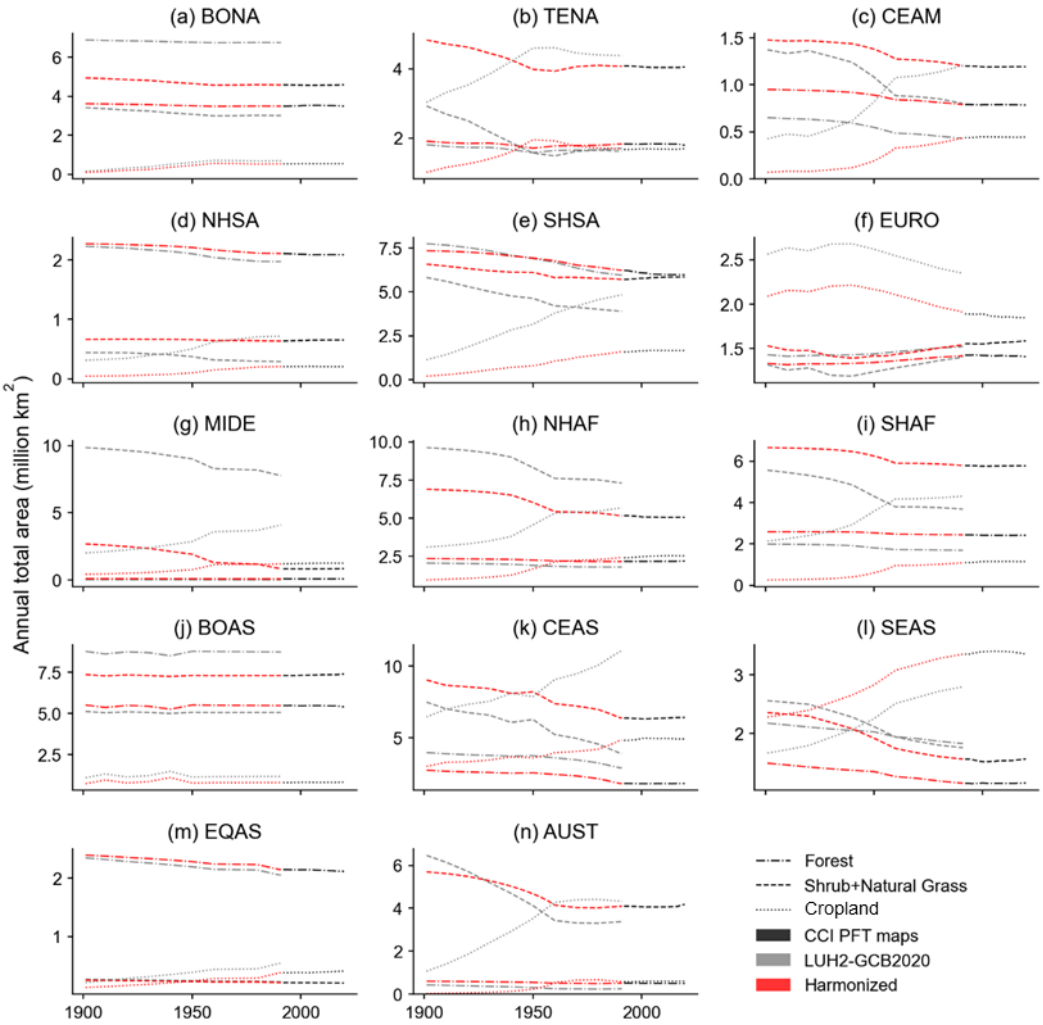

Figure S3. Time series of annual total area of different land use types using the CCI land cover maps (black), LUH2-GCB2020 (grey) and the harmonized data (red) in each region.

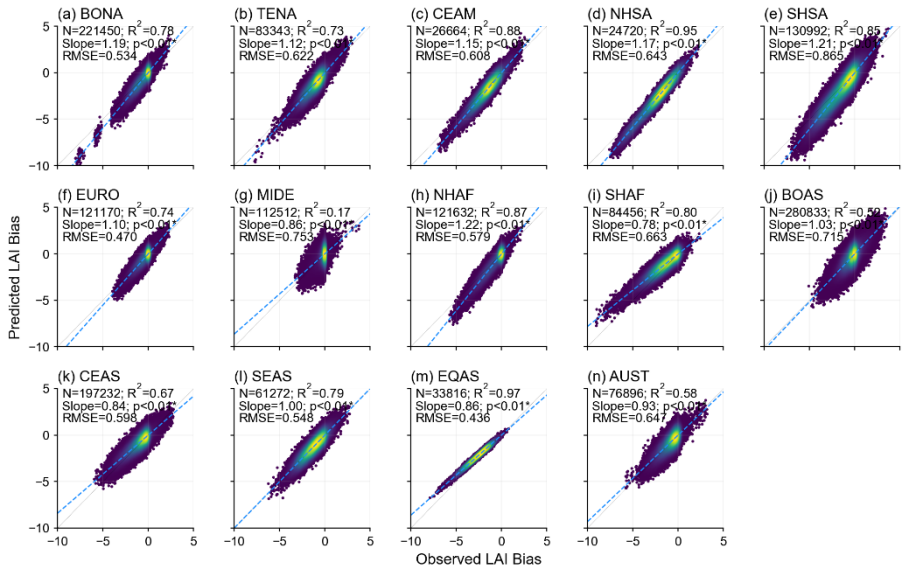

Figure S4. Evaluation of the LSTM regressions for predicting the LAI biases between GIMMS LAI4g and TRENDY v11 using the testing set (20%) of all years' data (1982-2020) in each region.

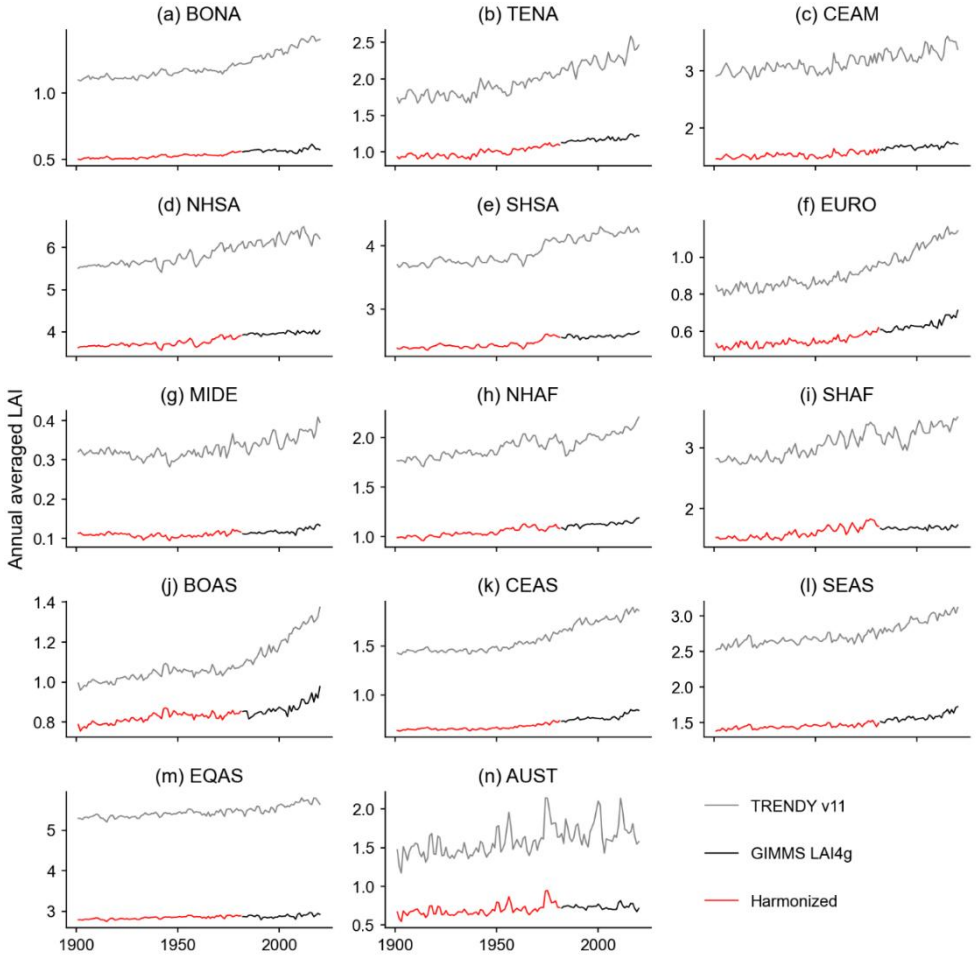

Figure S5. Time series of annual regional average LAI from GIMMS LAI4g (black), TRENDY v11 (grey) and the harmonized data (red) in each region.

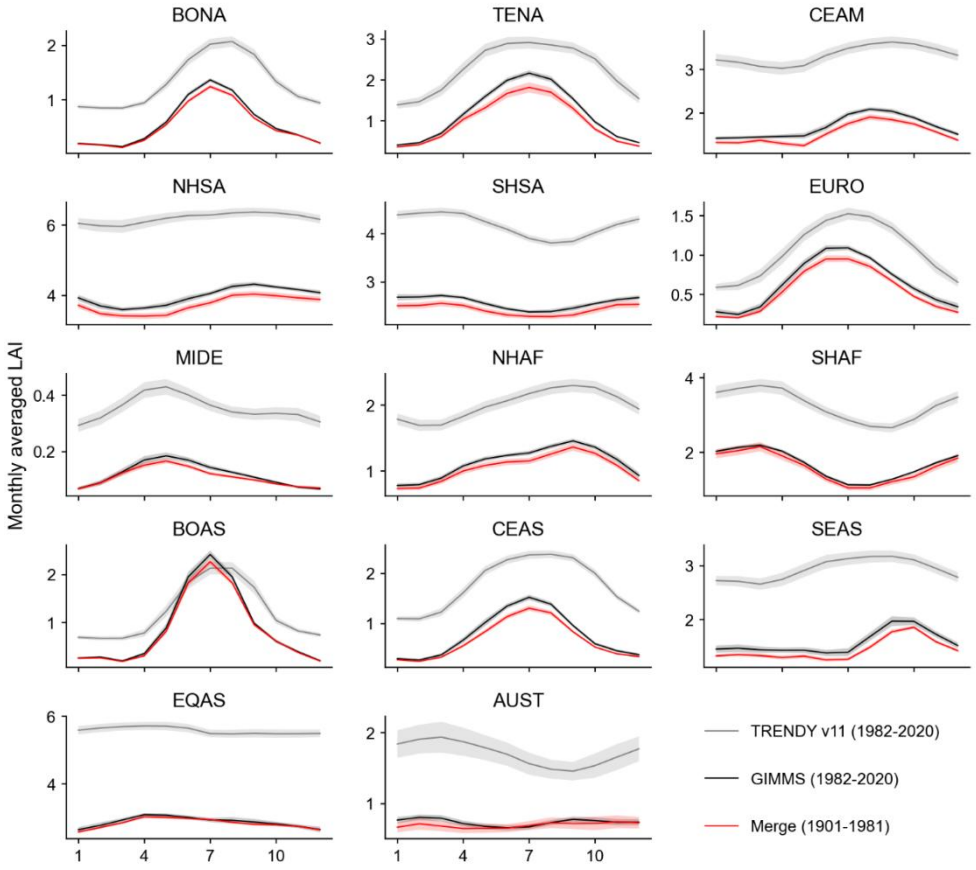

Figure S6. Seasonality of regional average LAI from GIMMS LAI4g (black), TRENDY v11 (grey) and the harmonized data (red) in each region.

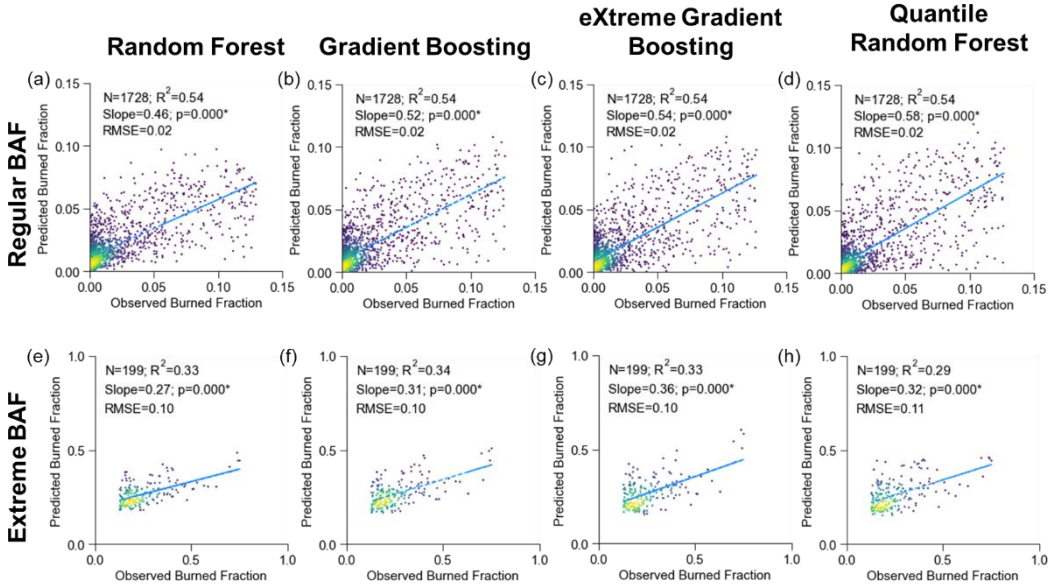

Figure S7. Evaluation of different machine learning regression models for regular (a-d) and extreme BAF (e-h), respectively using the testing set (20%) of 2010 in NHAF.

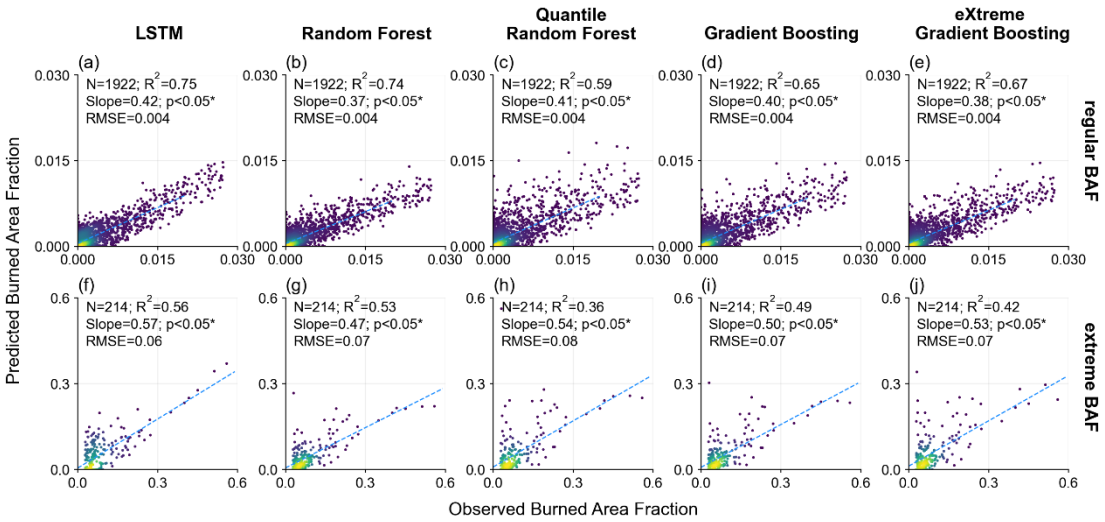

Fig. S8. Same as Fig. S7 but in BOAS. Evaluation of different machine learning regression models for regular (a-e) and extreme BAF (f-j), respectively using the testing set (20%) in 2010 in BOAS.

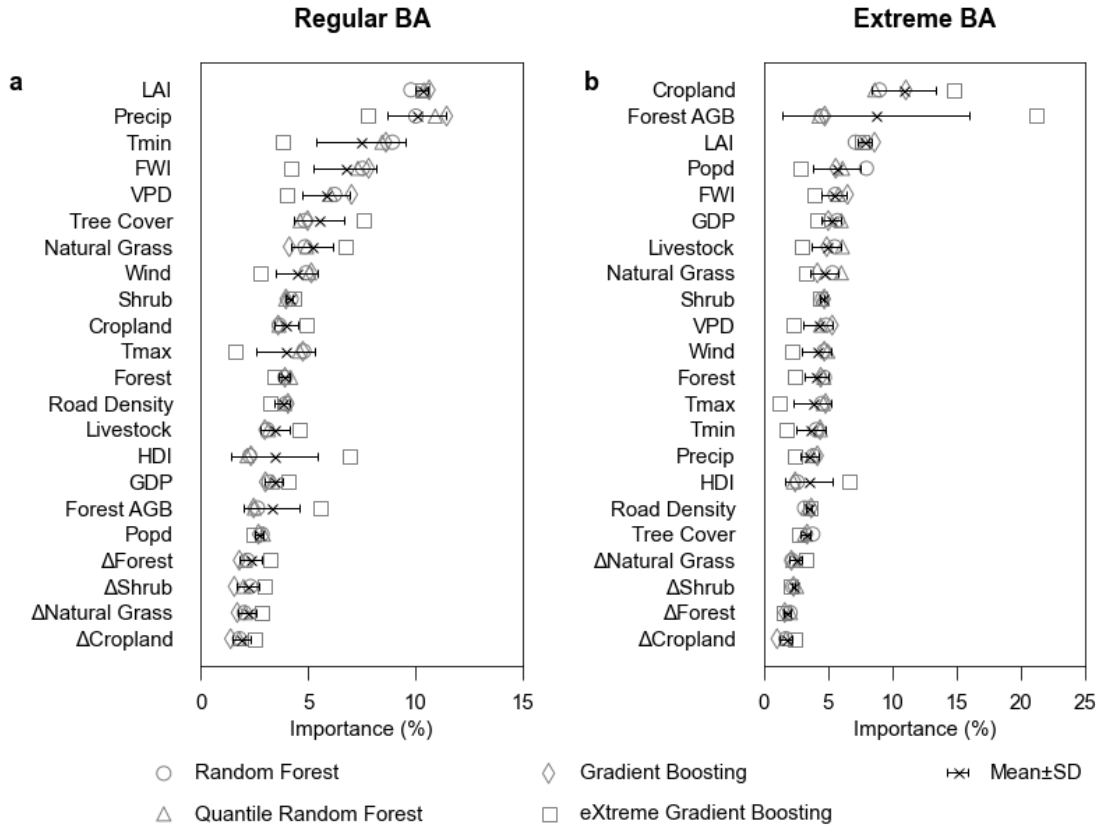

Figure S9. Feature importance for regular (a) and extreme BAF (b), respectively, in NHAF using different machine learning regression models.

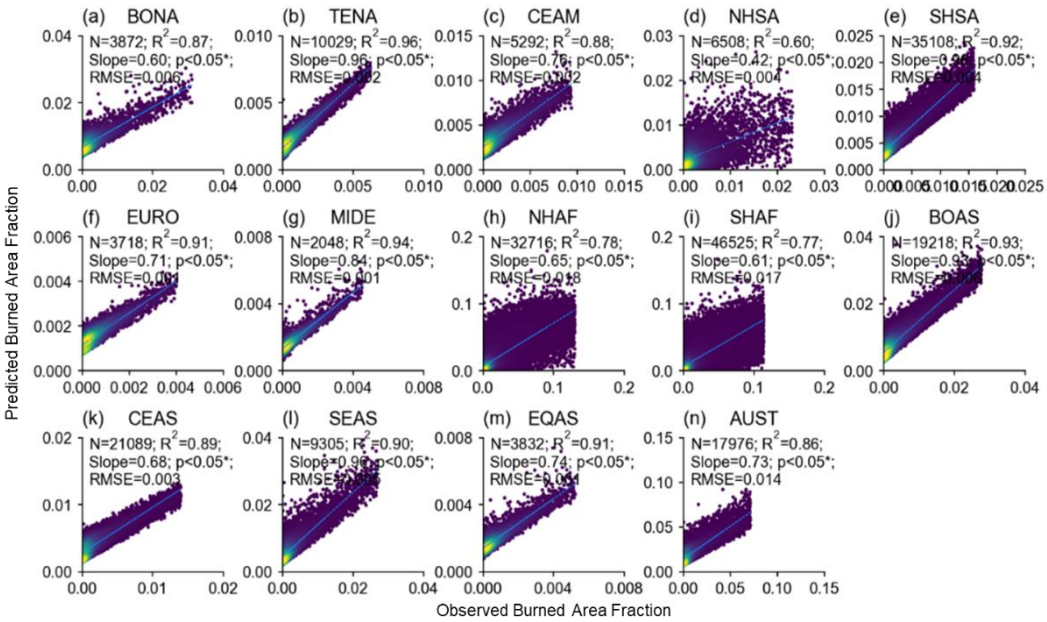

Figure S10. Evaluation of the LSTM regression models for the regular BAF using the testing set (20%) of all years' data (2003-2020) in each region.

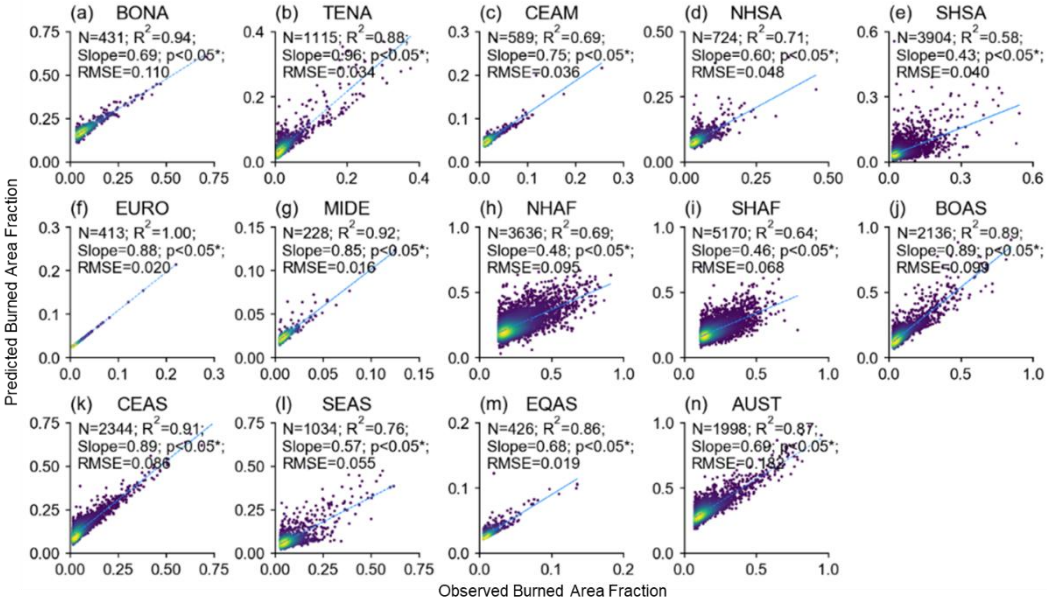

Figure S11. Same as Figure S10 but for extreme BAF.

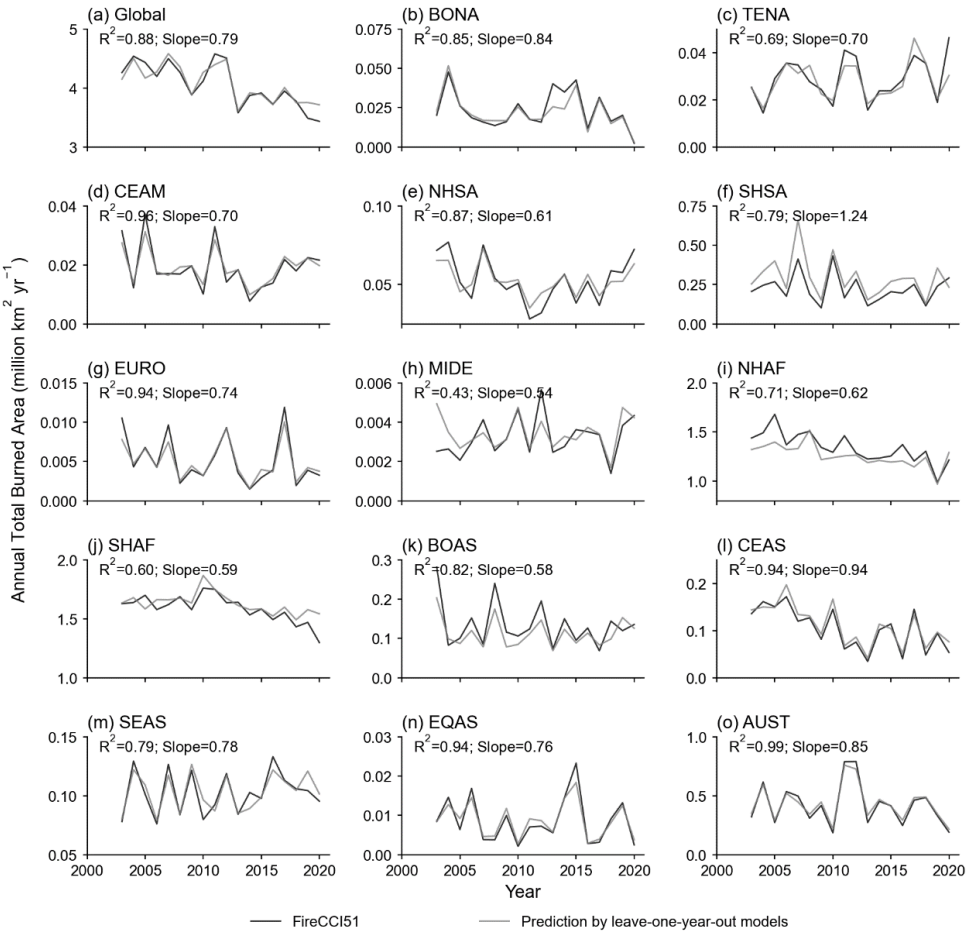

Figure S12. Time series of annual total burned area across the globe (a) and in each region (b-o) from FireCCI51 (black lines), and from predictions by the leave-one-year-out methods (grey lines). R^2 and slopes from the linear regressions between the two time series are also shown.

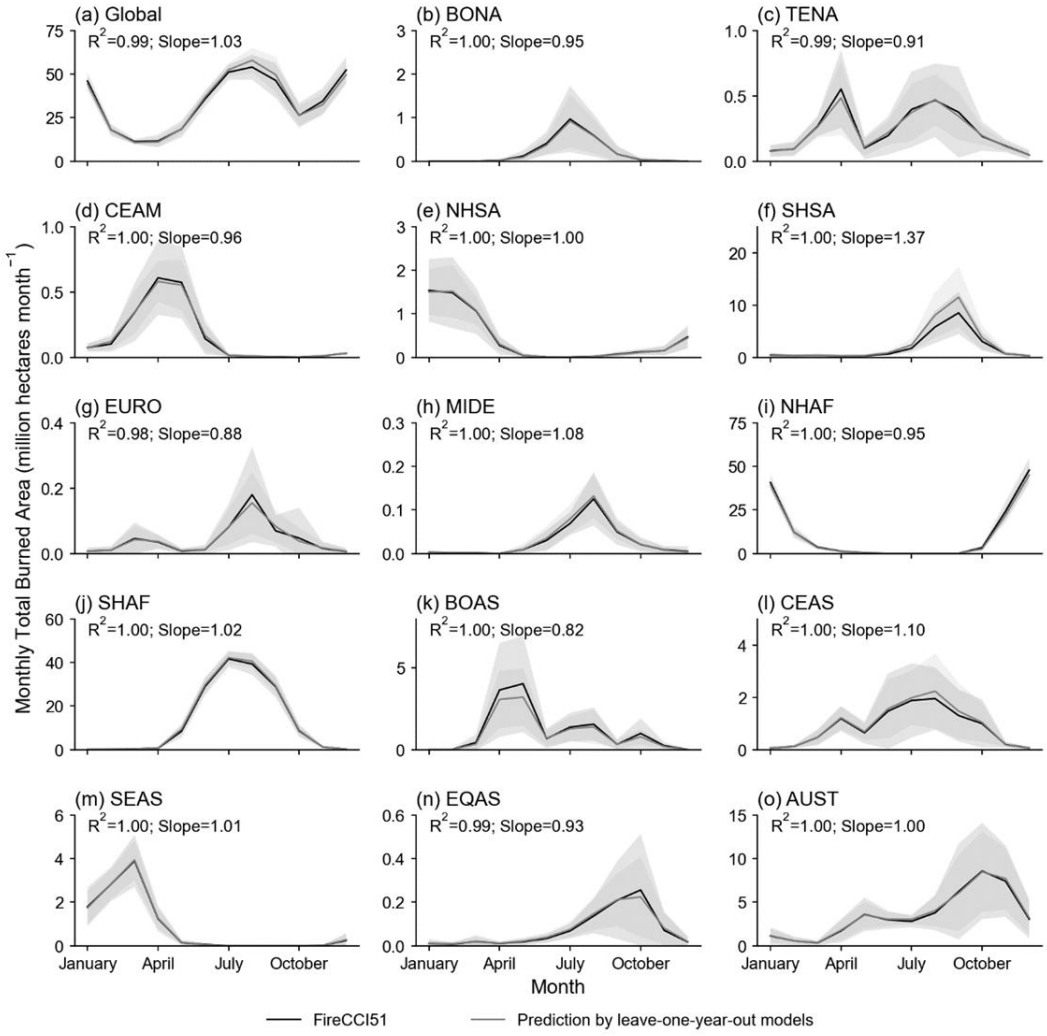

Figure S13. Seasonality of the total burned area at the global scale (a) and in each region (b-o) from FireCCI51 (2003-2020) and predictions by the leave-one-year-out methods (2003-2020). Lines and shaded area represent the average and standard deviation of monthly values across multiple years, respectively. R^2 and slopes from the linear regressions between the two time series are also shown.

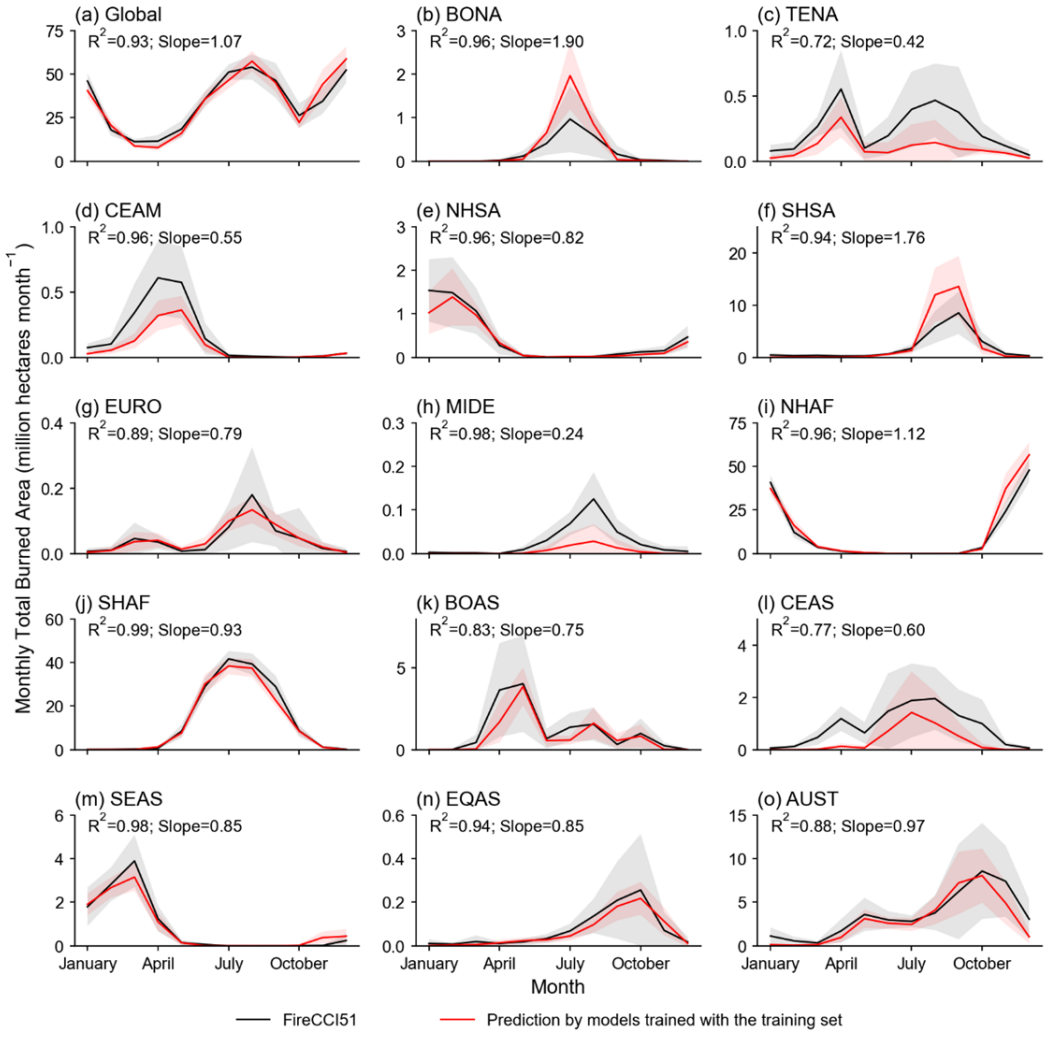

Figure S14. Same as Figure S13 but using predictions (1901-2020) by models trained with the training set (80% of all years' data during 2003-2020) instead. For the seasonality of the burned area, there are two peaks centered in August and December at the global scale (Fig. S14a). The December centered peak is mainly contributed NHAF (Fig. S14i), while the August peak mainly by SHSA and SHAF (Fig. S14f, S14j). Moreover, the monthly total burned area in 1901-2020 (red lines) are obviously lower than 2003-2020 (black lines) in TENA, CEAM, MIDE and CEAS (Fig. S14c, S14d, S14h, S14l), but apparently higher than 2003-2020 (black and grey lines) in BONA and SHSA (Fig. S14b, S14f).

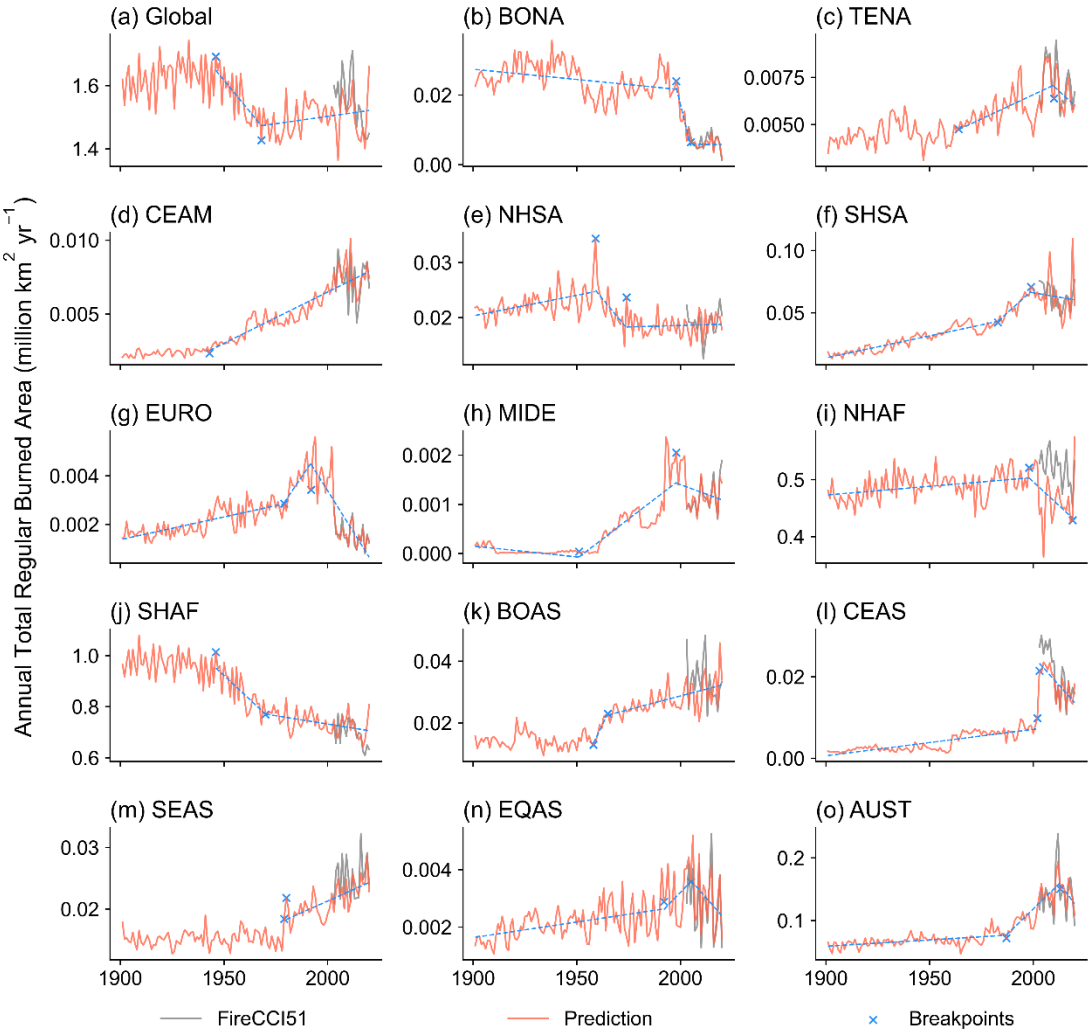

Figure S15. Time series of annual total burned area for regular fires across the globe (a) and in each region (b-o) from FireCCI51 (black lines, 2003-2020) and predictions (red lines, 1901-2020). The breakpoints and significant slopes (p-value < 0.05) in blue were also shown (Section 2.2 in the main text).

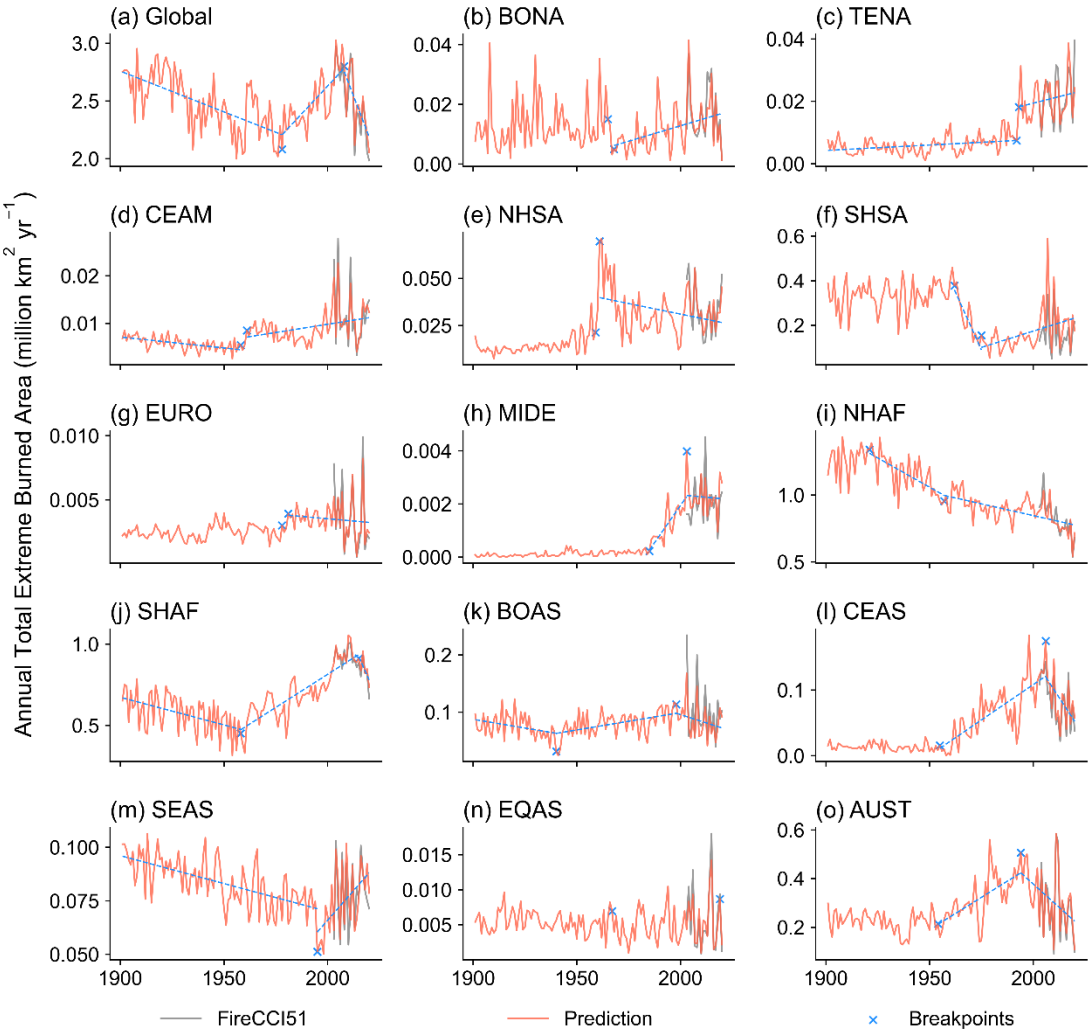

Figure S16. Same as Figure S15 but for extreme fires.

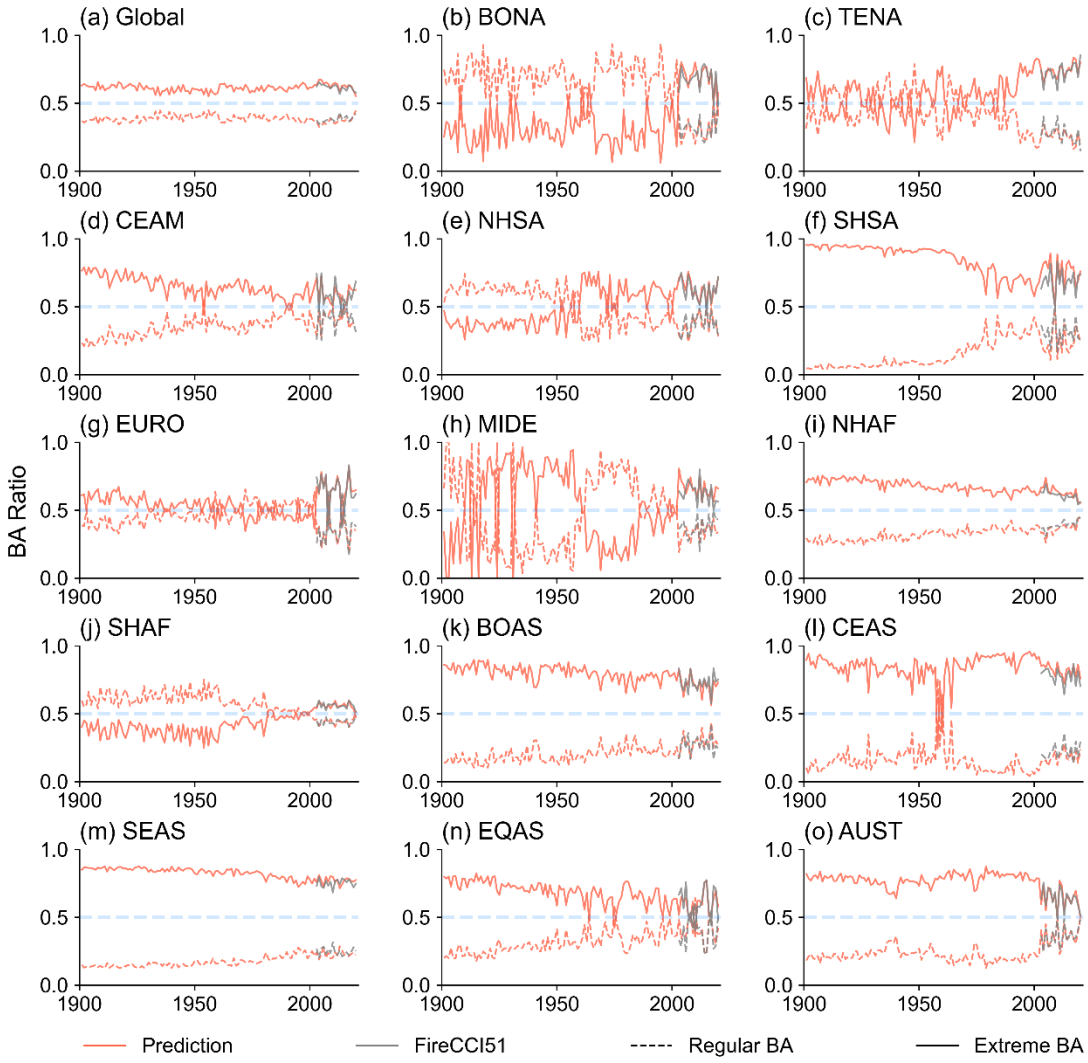

Figure S17. Time series of annual burned area ratios across the globe (a) and in each region (b-o) for regular (dashed lines) and extreme (solid lines) burned area from FireCCI51 (grey lines, 2003-2020) and predictions (red lines, 1901-2020). Burned area ratios of a certain fire type is calculated by the annual burned area of this fire type divided by the annual total burned area.

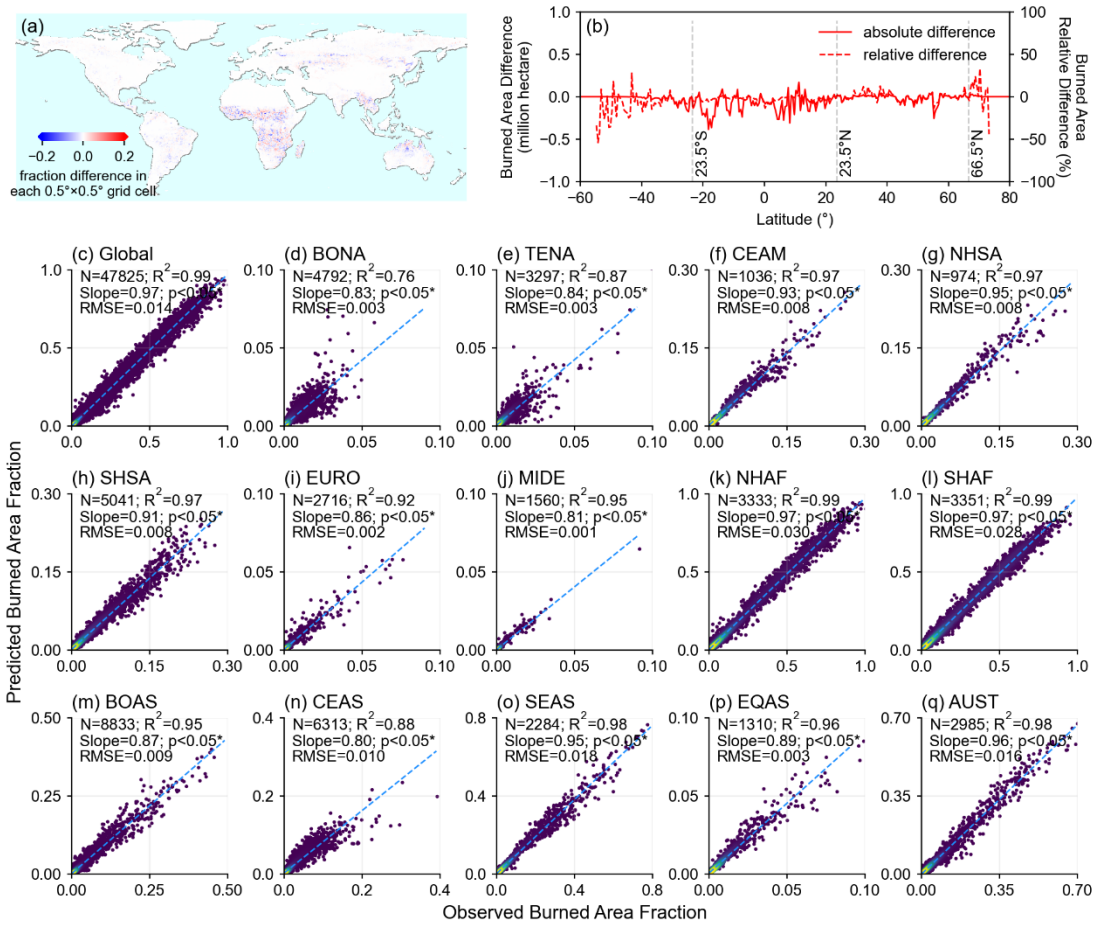

Figure S18. Evaluation of the multi-year (2003-2020) average burned area predicted from GFED5 against the GFED5 burned area using the leave-one-year-out method. (a) Map of burned area difference between predictions and GFED5 (the former minus the latter). (b) Latitudal sum of burned area difference using the area fraction difference map from (a) multiplied by the land area in each 0.5°×0.5° grid cell, where solid and dashed lines represent absolute and relative difference from the GFED5 observations. (c-q) Scatter plots of burned area fraction for each region from GFED5 and our predictions. RMSE represents rooted mean squared error between observations and predictions.

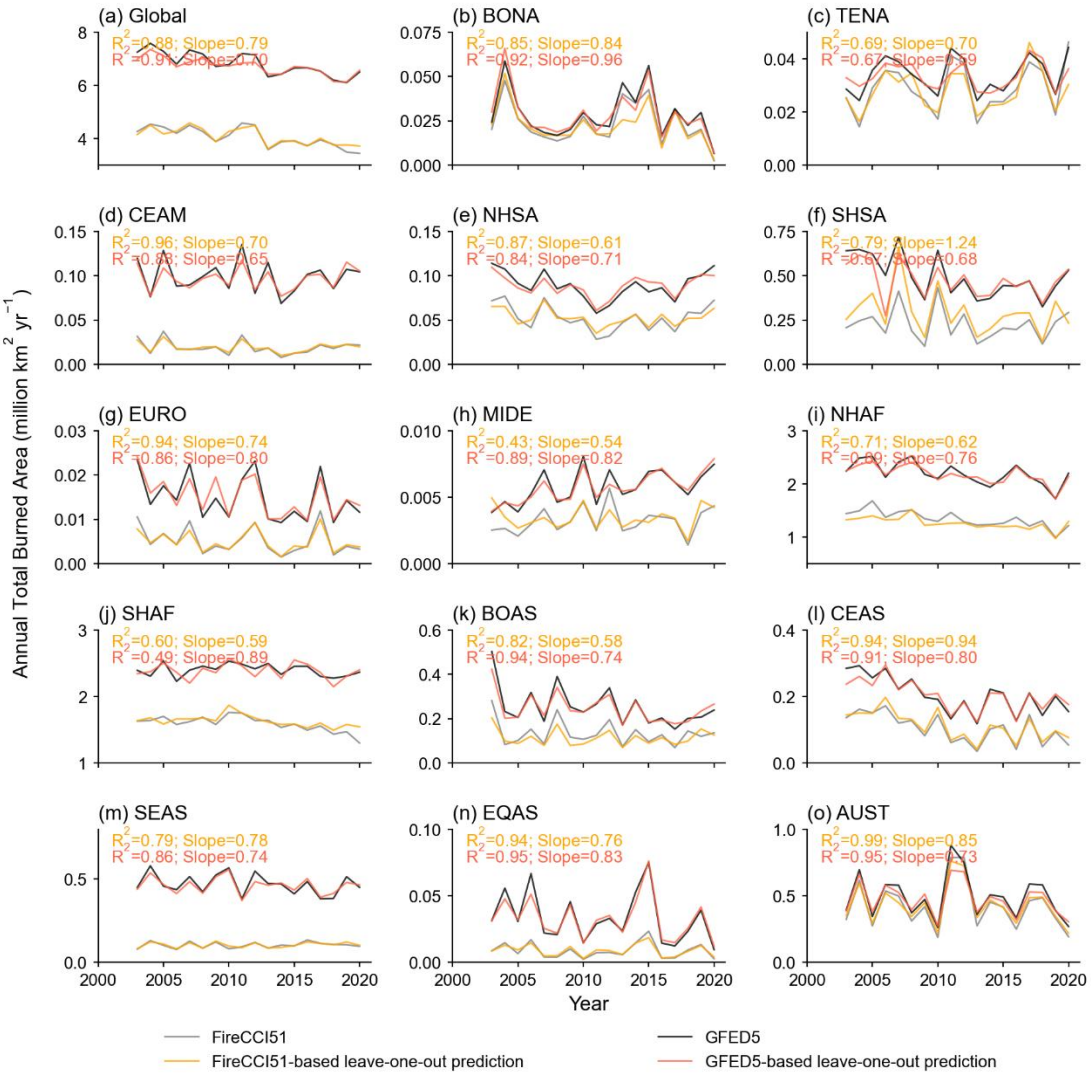

Figure S19. Time series of annual total burned area across the globe (a) and in each region (b-o) from FireCCI51 (grey lines) and GFED5 (black lines) observations, and from predictions by the leave-one-year-out methods based on FireCCI51 (orange lines) and GFED5 (red lines). R^2 and slopes from the linear regressions between observation and corresponding prediction are also shown.

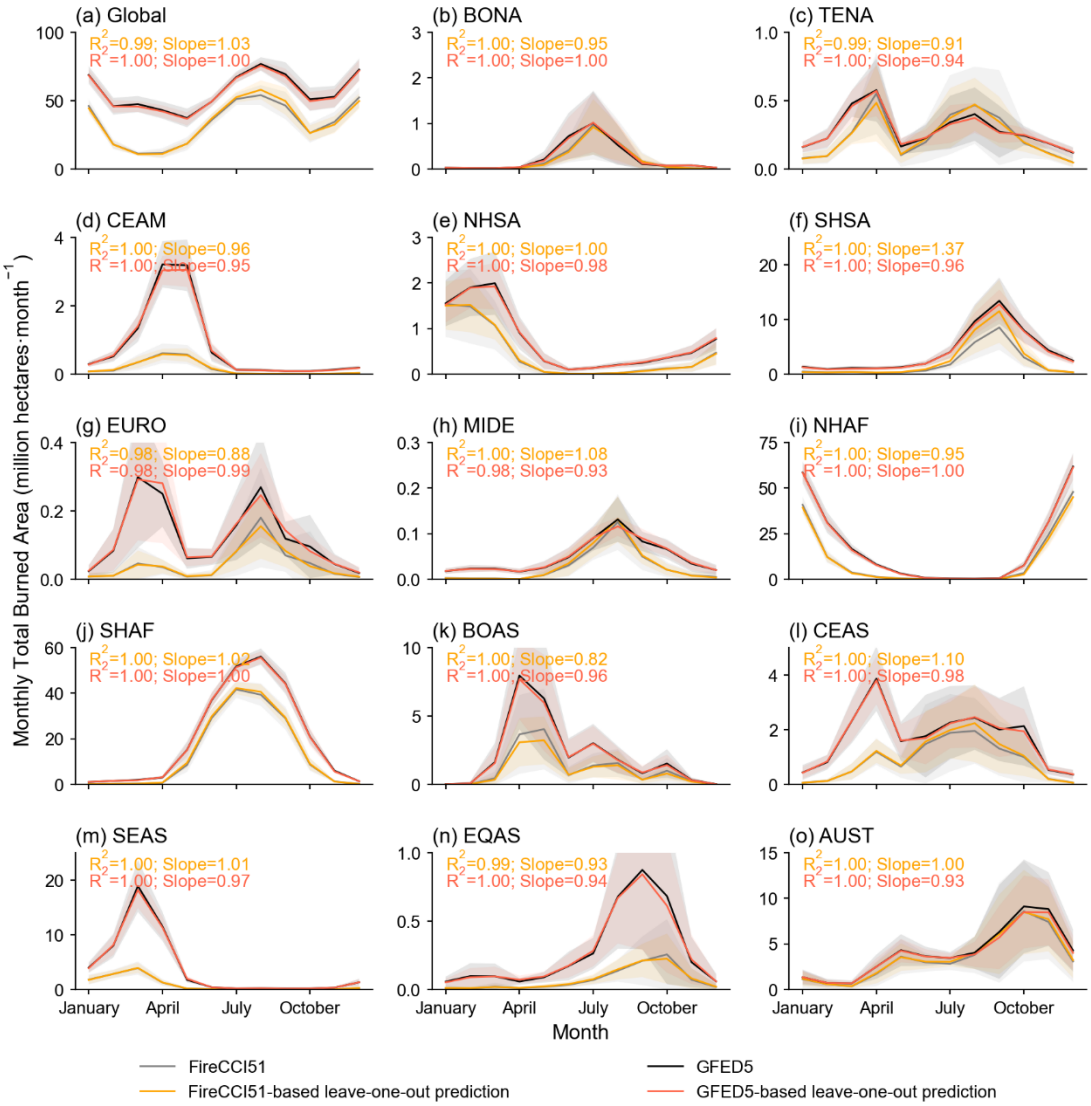

Figure S20. Seasonality of the total burned area (2003-2020) at the global scale (a) and in each region (b-o) from FireCCI51 (grey lines) and GFED5 (black lines), and predictions by the leave-one-year-out methods based on FireCCI51 (orange lines) and GFED5 (red lines). Lines and shaded area represent the average and standard deviation of monthly values across multiple years, respectively. R^2 and slopes from the linear regressions between observations and predictions are also shown.

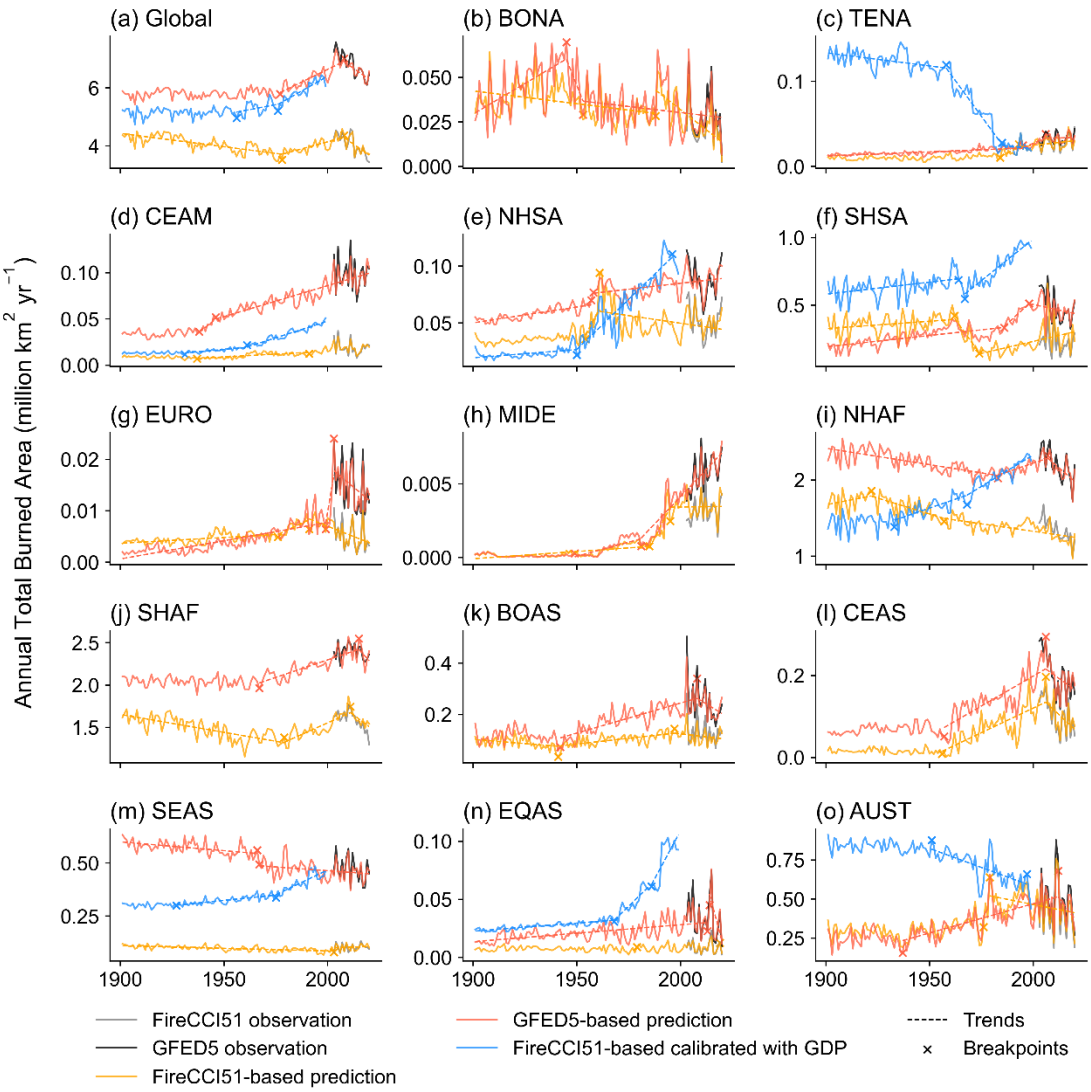

Figure S21. Time series of annual total burned area across the globe (a) and in each region (b-o) from FireCCI51 (grey lines, 2003-2020) and GFED5 (black lines, 2003-2020), and predictions based on FireCCI51 (orange lines, 1901-2020), GFED5 (red lines, 1901-2020) and calibrated with GDP before 2000 (blue lines, 1901-1999). The breakpoints and significant trends (dashed lines, p-value < 0.05) are also shown (Section 2.2 in the main text).

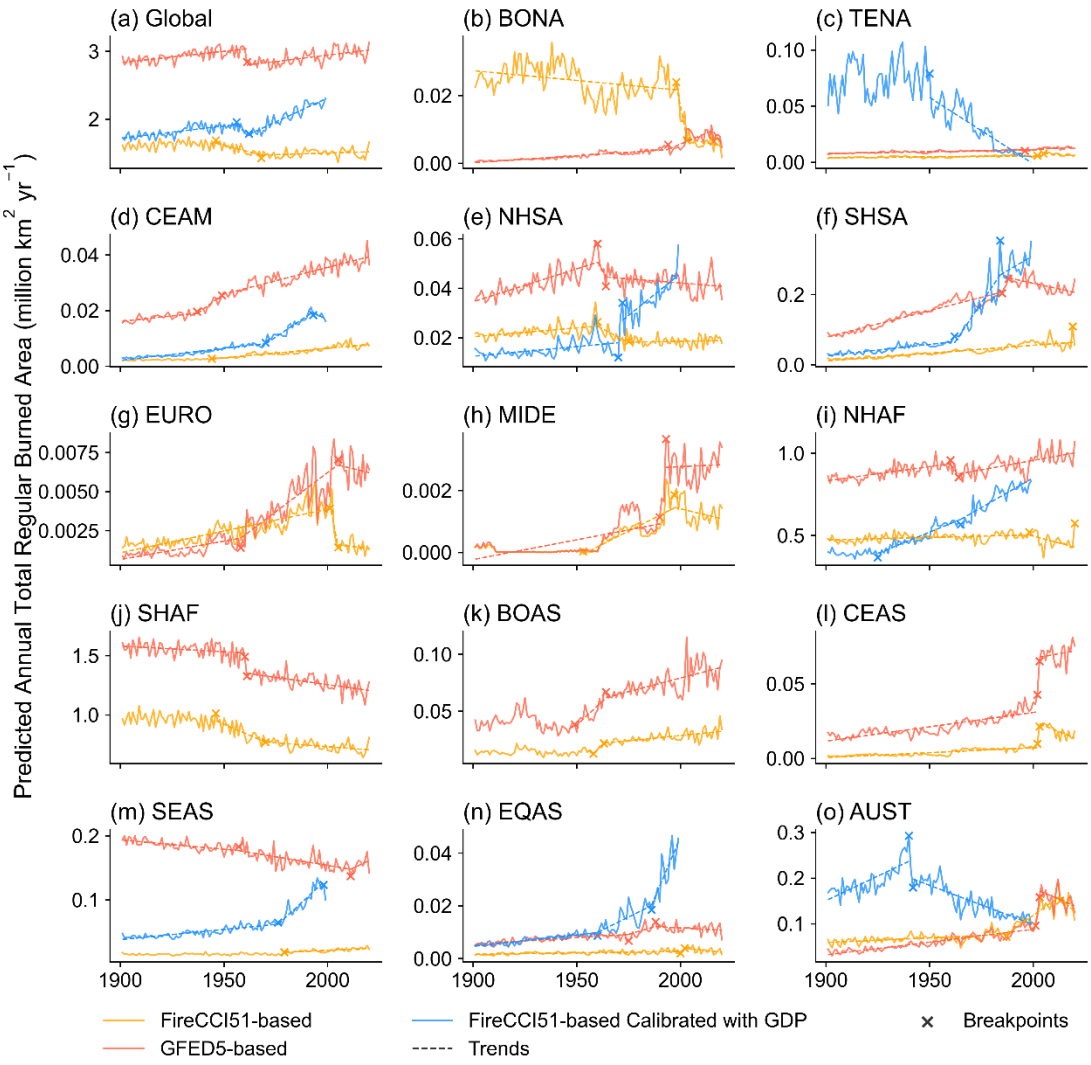

Figure S22. Time series of predicted annual total regular burned area across the globe (a) and in each region (b-o) from the original FireCCI51-based (orange lines, 1901-2020), GFED5-based (red lines, 1901-2020) and the FireCCI51-GDP (blue lines, 1901-1999) product versions. The breakpoints and significant trends (dashed lines, p-value < 0.05) are also shown (Section 2.2 in the main text).

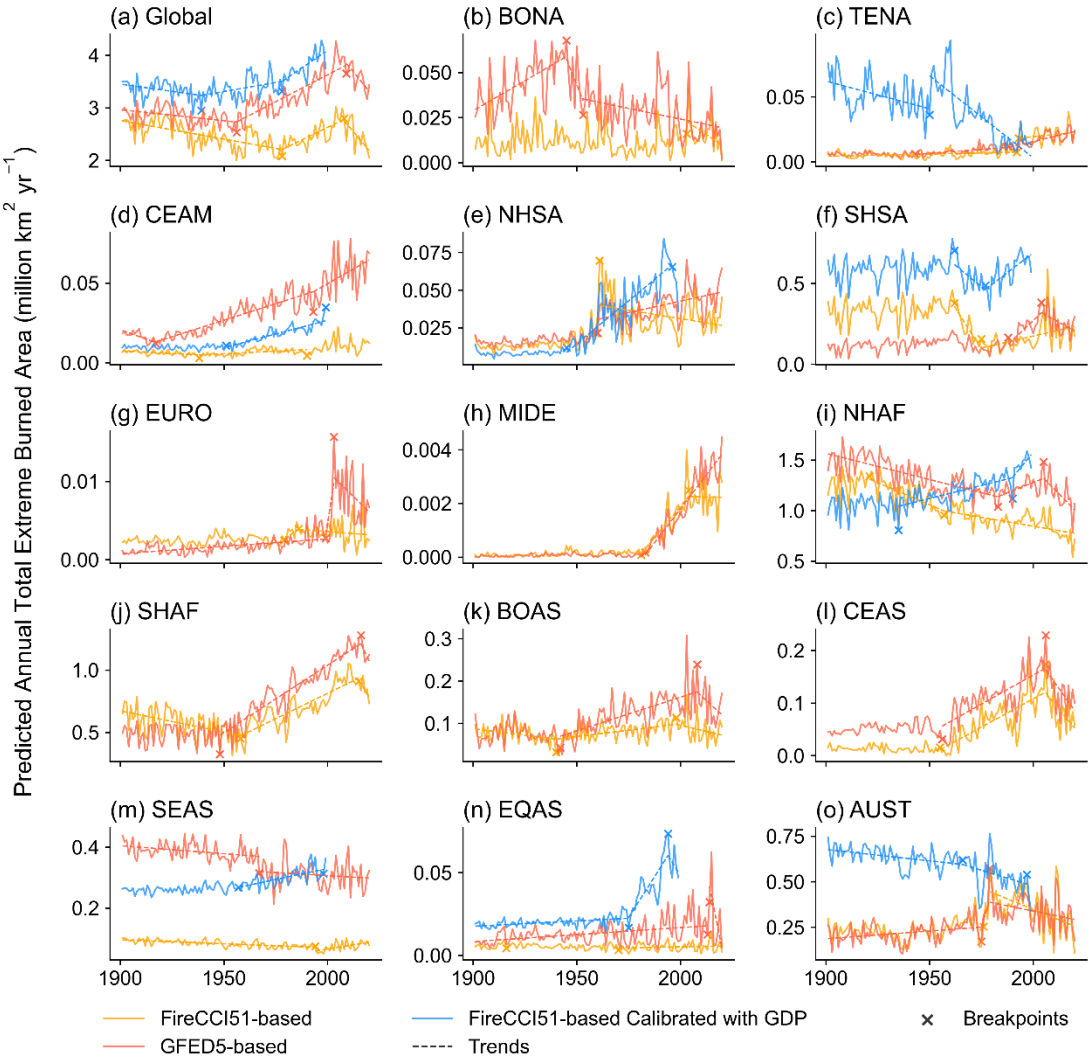

Figure S23. Same as Figure S22 but for extreme burned area.

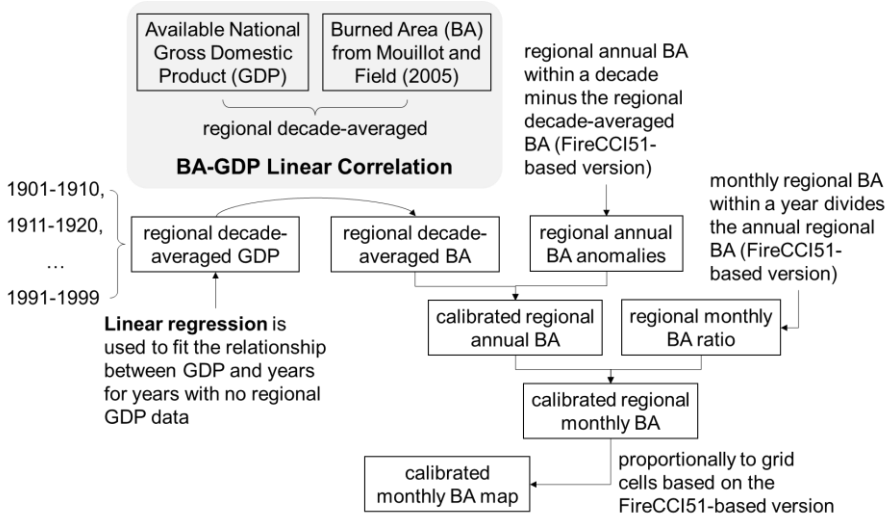

Figure S24. Workflow of calibrating the FireCCI51-based reconstruction burned area with GDP from the Maddison Project Database 2023 (Bolt and Van Zanden, 2024) and burned area from Mouillot and Field (2005) at the regional scale before 2000.

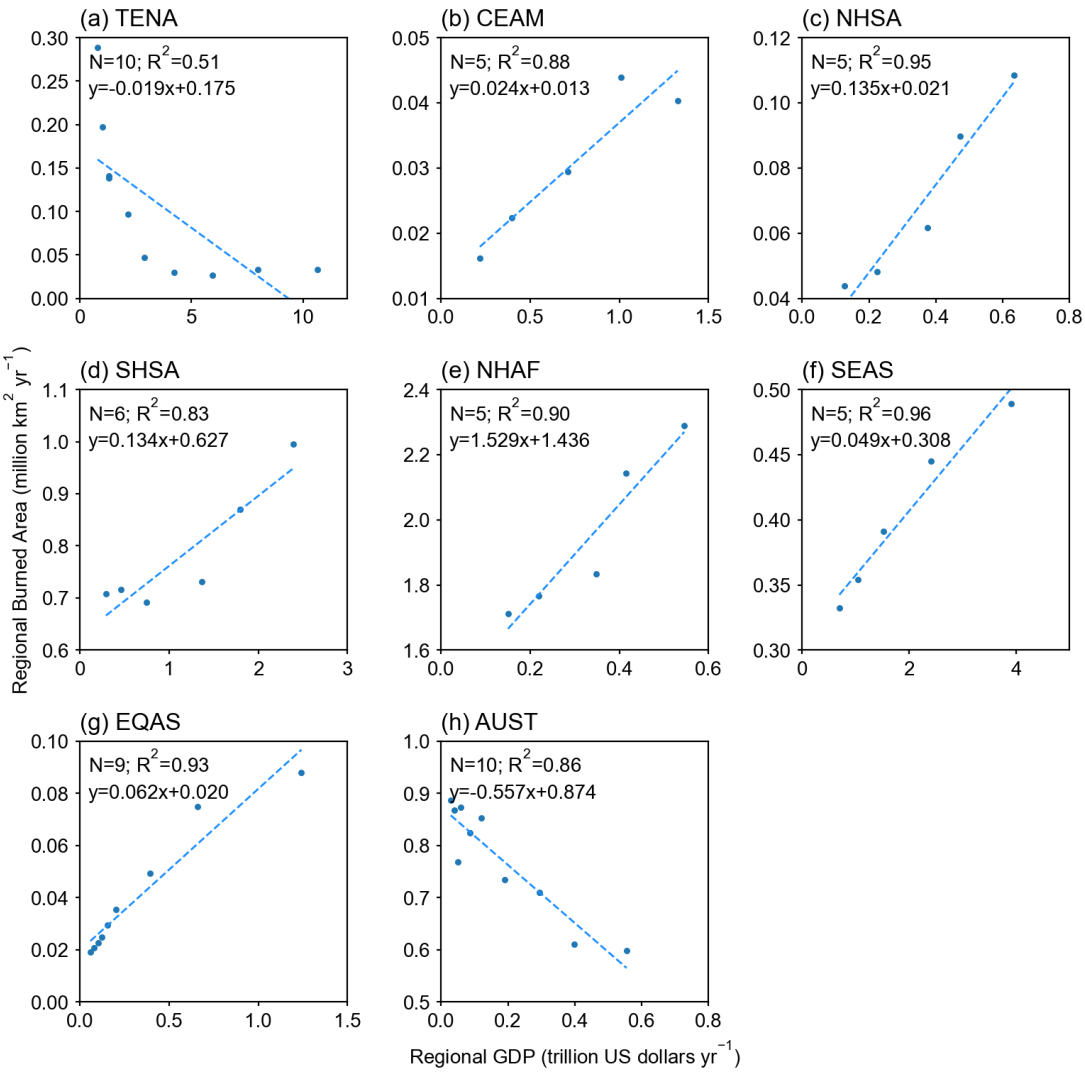

Figure S25. Correlations between the regional total decadal burned area from Mouillot and Field (2005) and GDP from the Maddison Project Database 2023 (Bolt and Van Zanden, 2024) in each region. Solid lines indicate the significant (p-value < 0.05) linear correlations, and dashed lines for non-significant.

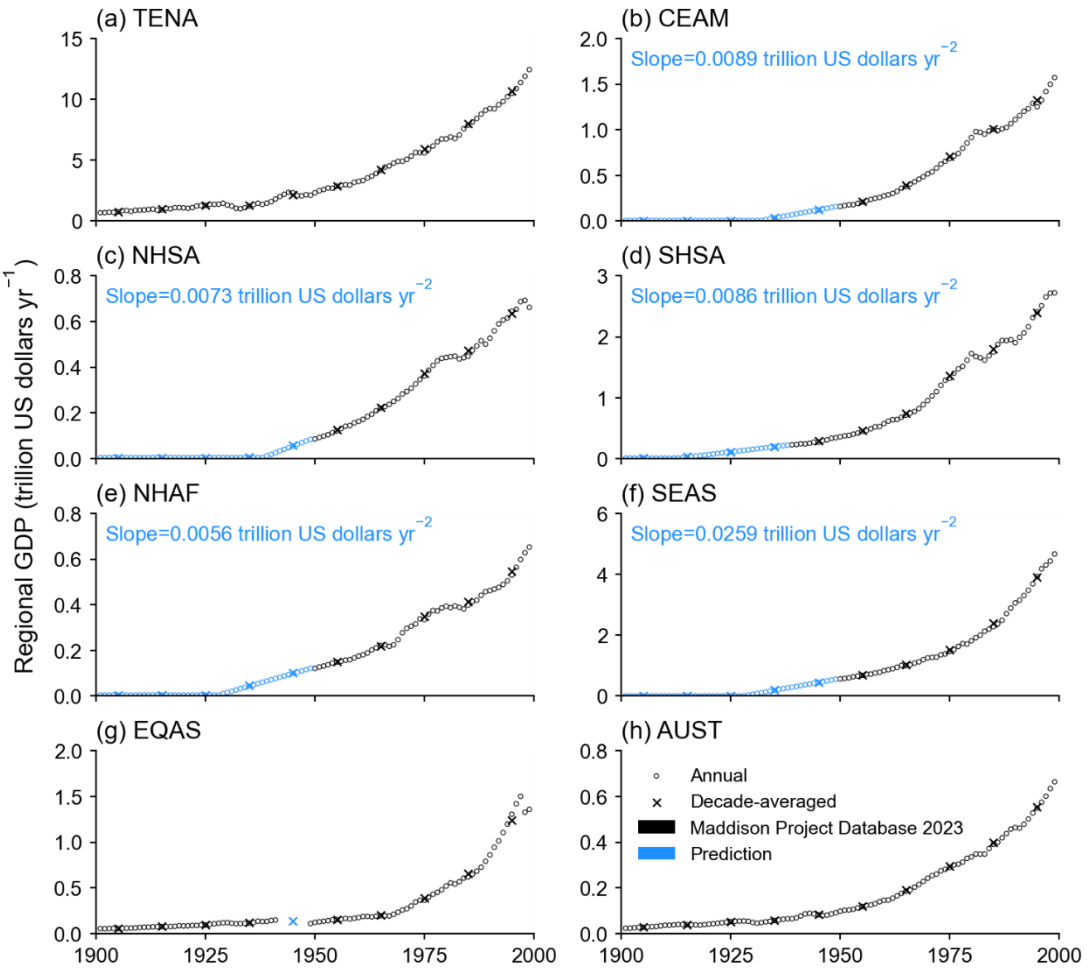

Figure S26. Time series of regional annual (circles) and decade-averaged (crosses) GDP from the Maddison Project Database 2023 (black) (Bolt and Van Zanden, 2024) and our reconstructed GDP (blue, see details below). Only regions with significant correlations (p-value < 0.05) in Figure S25 are shown here. In regions without annual GDP available before 1950, regional annual GDP in the earliest accessible 5 years were fitted against years using a linear regression. This regression was further applied to reconstruct the GDP in the earlier years. If the regional annual GDP was predicted to be negative by the linear regression, the regional annual GDP was assumed to be the same as the nearest year.

References

Bolt, J. and van Zanden, J. L.: Maddison-style estimates of the evolution of the world economy: A new 2023 update, Journal of Economic Surveys, n/a, https://doi.org/10.1111/joes.12618, 2024.

Bowman, D. M. J. S., Kolden, C. A., Abatzoglou, J. T., Johnston, F. H., van der Werf, G. R., and Flannigan, M.: Vegetation fires in the Anthropocene, Nature Reviews Earth & Environment, 1, 500-515, 10.1038/s43017-020-0085-3, 2020.

Bowman, D. M. J. S., Balch, J. K., Artaxo, P., Bond, W. J., Carlson, J. M., Cochrane, M. A., D'Antonio, C. M., DeFries, R. S., Doyle, J. C., Harrison, S. P., Johnston, F. H., Keeley, J. E., Krawchuk, M. A., Kull, C. A., Marston, J. B., Moritz, M. A., Prentice, I. C., Roos, C. I., Scott, A. C., Swetnam, T. W., van der Werf, G. R., and Pyne, S. J.: Fire in the Earth System, Science, 324, 481-484, 10.1126/science.1163886, 2009.

Cary, G. J., Keane, R. E., Gardner, R. H., Lavorel, S., Flannigan, M. D., Davies, I. D., Li, C., Lenihan, J. M., Rupp, T. S., and Mouillot, F.: Comparison of the Sensitivity of Landscape-fire-succession Models to Variation in Terrain, Fuel Pattern, Climate and Weather, Landscape Ecology, 21, 121-137, 10.1007/s10980-005-7302-9, 2006.

Danielson, J. J. and Gesch, D. B.: Global multi-resolution terrain elevation data 2010 (GMTED2010), Report 2011-1073, 10.3133/ofr20111073, 2011.

Kaplan, J. O. and Lau, K. H. K.: The WGLC global gridded lightning climatology and time series, Earth Syst. Sci. Data, 13, 3219-3237, 10.5194/essd-13-3219-2021, 2021.

Mouillot, F. and Field, C. B.: Fire history and the global carbon budget: a 1°× 1° fire history reconstruction for the 20th century, Global Change Biology, 11, 398-420, https://doi.org/10.1111/j.1365-2486.2005.00920.x, 2005.

van der Werf, G. R., Randerson, J. T., Giglio, L., van Leeuwen, T. T., Chen, Y., Rogers, B. M., Mu, M., van Marle, M. J. E., Morton, D. C., Collatz, G. J., Yokelson, R. J., and Kasibhatla, P. S.: Global fire emissions estimates during 1997–2016, Earth Syst. Sci. Data, 9, 697-720, 10.5194/essd-9-697-2017, 2017.